



# Niobium single-atom catalyst implanted three-dimensional ordered porous carbon nanofibers as an active sulfur host for efficient lithium-sulfur batteries

Shufeng Jia<sup>a,1</sup>, Shupeng Zhao<sup>b,1</sup>, Zijing Xu<sup>c</sup>, Chuyin Ma<sup>b</sup>, Tingzhou Yang<sup>c,\*</sup>, Lining Pan<sup>d</sup>, Jiabing Liu<sup>a</sup>, Yan Wang<sup>a</sup>, Tongbin Zhang<sup>a</sup>, Xia Sun<sup>a</sup>, Ning Liu<sup>a,\*</sup>, Yongguang Zhang<sup>a,\*</sup>, Zhongwei Chen<sup>c</sup>

<sup>a</sup> School of Materials Science and Engineering, Hebei University of Technology, Tianjin 300130, China

<sup>b</sup> Institute of Carbon Neutrality, Zhejiang Wanli University, Ningbo 315100, China

<sup>c</sup> Department of Chemical Engineering, Waterloo Institute for Nanotechnology University of Waterloo, Waterloo, ON N2L 3G1, Canada

<sup>d</sup> Sunyes Shanshan Advanced Materials Technology Co., Ltd, Quzhou 324000, China

<sup>e</sup> Centre for Energy (M473), The University of Western Australia, 35 Stirling Highway, Crawley, WA 6009, Australia

## ARTICLE INFO

### Keywords:

Lithium-sulfur batteries  
Single atom catalyst  
3D-ordered porous structure  
Electrocatalysts  
Lithium polysulfide

## ABSTRACT

The lithium-sulfur (Li-S) battery is one of the most potential next-generation energy storage devices, but the insulating properties of the sulfur cathode, the detrimental shuttle effect of lithium polysulfide, and the volume change during cycling hinder their commercial viability. Herein, we report a uniquely designed sulfur host based on well-dispersed single Nb atom catalysts with 3D-ordered porous carbon nanofibers (Nb-SAs@3DOP-C) by a simple chemical polymerization method from porous anodic aluminum oxide templates. The 3D-ordered porous carbon nanofibers provide a physical barrier for the shuttle effect and an open framework to efficiently boost the utilization of sulfur species. Introducing single Nb atoms possess relatively higher binding energy for polysulfide intermediate, showing excellent charge transfer/kinetic toward sulfur redox. As a result, the S/Nb-SAs@3DOP-C composite delivers a satisfactory discharge capacity of 1208.1 mAh g<sup>-1</sup> and an ultra-low capacity decay of 0.012% per cycle over 500 cycles. This work may provide new insights into single atom-decorated 3D porous materials for enhancing electrochemical performance of advanced Li-S battery for energy storage and conversion.

## 1. Introduction

With the growing demand for high-energy-density storage devices, the exploration of next-generation battery systems has attracted great attention[1,2]. Among them, Li-S battery exhibits great potential as one of the energy-intensive applications due to its low cost, natural abundance, and high theoretical specific capacity[3,4]. Despite these promising advantages, several issues still need to be solved before the large-scale commercial application[5–7]. The exploration of high-performance Li-S batteries is still hampered by a multitude of thorny issues[8], including the sluggish S redox kinetics[9,10], shuttle effect induced by soluble polysulfides[11], and volume expansion during cycles, further limiting the delivered capacity and capabilities[12]. Up to date, various strategies have been dedicated to addressing the

above-mentioned challenges, such as designing unique host materials [13–16], optimizing the electrolyte composition[17,18], employing functional interlayers[19–21], etc.

It is well known that the incorporation of highly conductive carbon materials with the porous structure as the S host can effectively improve the performance of Li-S batteries[22–26]. Unfortunately, these carbon materials are not sufficient to completely prevent the shuttle effect due to the weak van der Waals force with the polar lithium polysulfide molecules, and the irreversible loss of the active substance still exists during prolonged cycling[27]. Therefore, it is necessary to introduce efficient catalytic sites to enhance the catalytic activity. Due to their maximized exposed atomic efficiency, special size quantum effects, and unique electronic structure, single-atom catalysts (SACs) with individual metal centers have been developed for electrocatalysis[28–31].

\* Corresponding authors.

E-mail addresses: [t43yang@uwaterloo.ca](mailto:t43yang@uwaterloo.ca) (T. Yang), [ningliu1985@hebut.edu.cn](mailto:ningliu1985@hebut.edu.cn) (N. Liu), [yongguangzhang@hebut.edu.cn](mailto:yongguangzhang@hebut.edu.cn) (Y. Zhang).

<sup>1</sup> These authors contributed equally to this work.

Although some strategies show significant catalytic activity and selectivity, they cannot solve the problem of regulating the local atomic structure and controlling the loading of SACs. Furthermore, the relatively high manufacturing costs for single-atom catalysts further limit the pace of commercialization. Compared with V and Ta elements, the unique electronic configuration of the single Niobium (Nb) atom with one empty orbital and five half-occupied orbitals ( $4d^4 5s^1$ ) endows the system with excellent adsorption-desorption capacity in the vanadium subgroup and catalytic stability for reduction reactions[32–35]. Therefore, combining the strategies of carbon materials and Nb-SAs composite material is a chance to obtain an extraordinary cathode material for Li-S batteries.

Herein, the Nb Single-atom anchored wire-like three-dimensional ordered porous carbon nanofibers are reported as an advanced sulfur immobilizer in Li-S batteries. The ordered porous structure with suitable interconnected large pores, highly opened surfaces, and sufficient exposure sites can provide aster mass transfer properties, and the introduced Nb-C<sub>3</sub> coordinated moieties service as catalytic active sites to reduce the energy barrier of the Li<sub>2</sub>S oxidation reactions, further

promoting the redox kinetics of Li-S batteries. As a result, the S/Nb-SAs@3DOP-C composite delivers an initial discharging capacity of 1208.1 mAh g<sup>-1</sup> and an ultra-low capacity decay of 0.012% per cycle at 1.0 C over 500 cycles. Our work offers an efficient strategy to couple the 3D-ordered porous carbon nanowire substrate and single-atom catalysts for high-energy-density Li-S batteries.

## 2. Results and Discussion

Fig. 1a shows the schematic diagram of the preparation process for the Nb-SAs@3DOP-C composite. By wetting silica nanospheres into the nanopores of AAO templates (Fig. S1), the tubular ordered structure of the AAO template is closely and uniformly filled by the silica nanospheres. A high-temperature annealing process is used to obtain Nb-SAs@3DOP-C and 3DOP-C nanofiber array with a diameter of 250 nm (Fig. 1b and S2). From SEM cross-sectional images, the Nb-SAs@3DOP-C composite exhibits a nanofiber architecture with a neat and uniform length of 70  $\mu$ m (Fig. S3). The single Nb atom catalysts were introduced into the wire-like 3D-ordered porous carbon nanofibers, further

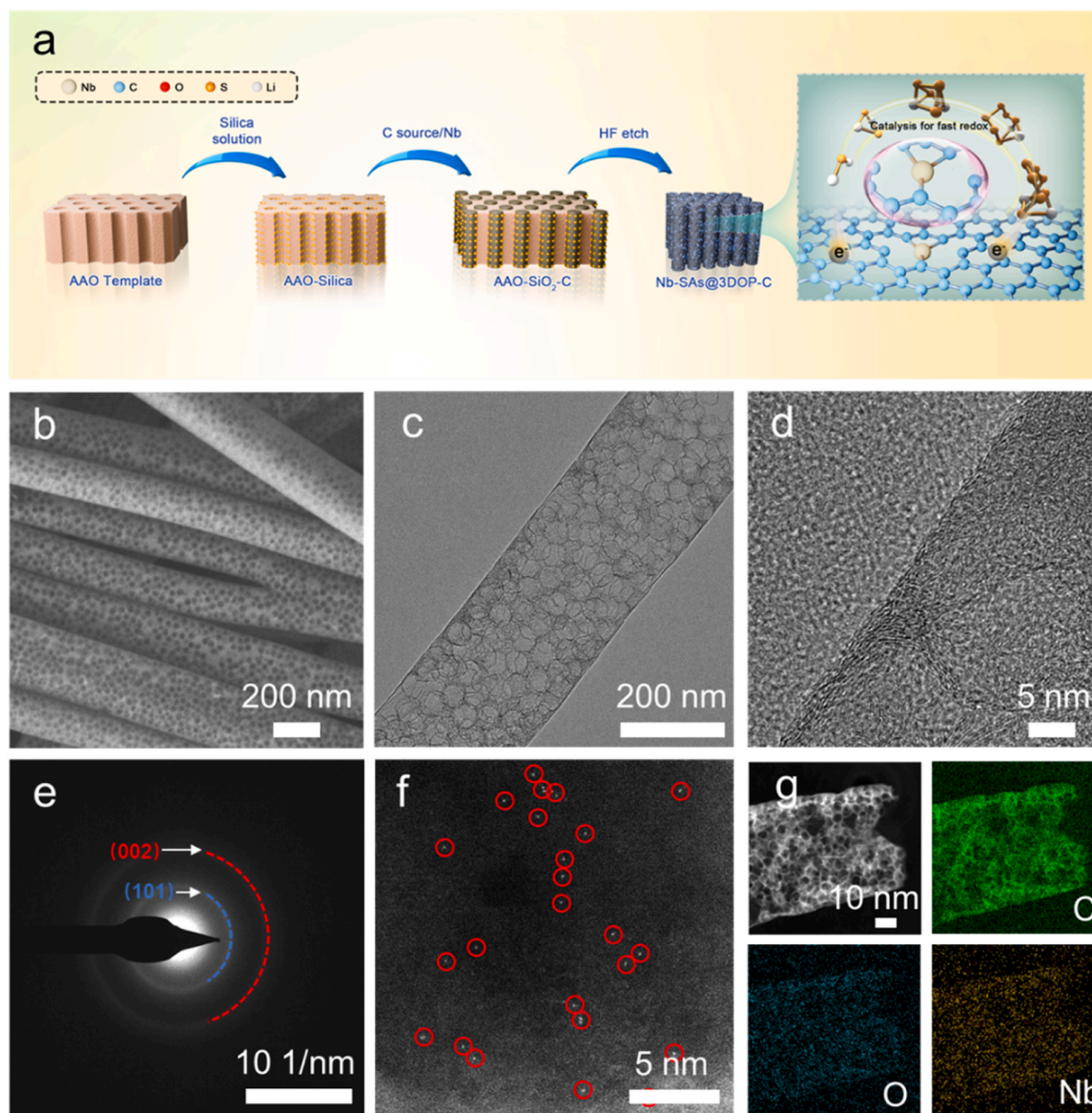


**Fig. 1.** (a) The Schematic illustration of the synthesis process of Nb-SAs@3DOP-C composite; (b) SEM image of Nb-SAs@3DOP-C nanofiber; (c) TEM images, (d) HRTEM images, and (e) SAED pattern of Nb-SAs@3DOP-C nanofiber. (f) High resolution HAADF-STEM pattern and (g) EDS mapping images of Nb-SAs@3DOP-C nanofiber.

accelerating the electron transport during the electrochemical catalytic reaction. At the same time, the oxygen vacancy interacted with single Nb atoms exhibit strong adsorption of lithium polysulfides (LiPSs), further promoting the conversion of sulfur species. As shown in TEM and high-resolution TEM (HRTEM) images (Fig. 1c, d), the distinct and orderly porous carbon structure of Nb-SAs@3DOP-C provided abundant active sites to disperse Nb single-atoms without any collapsed or missing structures. The increase in interfacial activity enhanced the physical adsorption of the composite to the LiPSs.

To explore the atomic structure and the existing form of Nb atoms, the aberration-corrected high-angle annular dark-field scanning transmission electron microscopy (HAADF-STEM) image clearly confirmed that a large amount of bright spots corresponding to Nb single atoms were uniformly distributed on the surface and inside Nb-SAs@3DOP-C nanofibers (highlighted with red circles, Fig. 1f), confirming the successful synthesis of single Nb atoms. Meanwhile, the elemental distribution was analyzed by energy dispersive spectroscopy (EDS). As displayed in Fig. 1g, the Nb elements were uniformly distributed within the carbon nanofiber with an element content of 1.13%. The XRD patterns of the 3DOP-C nanofibers, Nb-SAs@3DOP-C, and S/Nb-SAs@3DOP-C samples are shown in Fig. 2a. Among them, a broad diffraction peak can be observed at around  $23^\circ$  for Nb-SAs@3DOP-C,

corresponding to the characteristic peak of common carbon nanofibers.[36] As shown in Fig. S4, the  $N_2$  adsorption/desorption isotherms and corresponding pore distribution measurements of Nb-SAs@3DOP-C and 3DOP-C were investigated. The results showed that Nb-SAs@3DOP-C composite has a relatively large specific surface area of  $378.8 \text{ m}^2 \text{ g}^{-1}$ , which can effectively increase the contact area between electrodes and polysulfides with a high ionic conductivity and enable a high sulfur content of about 74% (Fig. S5). Moreover, the bonding of single Nb atoms could effectively improve the 3D ordered porous, thereby enhancing the significant catalytic effect on 3DOP-C nanofibers.

The corresponding Raman spectra of Nb-SAs@3DOP-C display two broad peaks located at  $1339$  and  $1589 \text{ cm}^{-1}$ , corresponding to the D-band produced by disoriented carbon and G-band originated from  $\text{sp}^2$  carbon atom pairs, respectively (Fig. S6). The degree of reduction in crystallization of the carbon material was evaluated by comparing the intensity ratio of the D and G peaks ( $I_D/I_G$ ) of each sample. Compared with 3DOP-C, Nb-SAs@3DOP-C exhibited a higher  $I_D/I_G$  intensity ratio of 0.94, which is caused by the defects appearing in the crystal planes due to the elimination of oxygen groups in the crystalline structure and the increase of number of  $\text{sp}^2$  bonds between the carbon atoms, revealing the successful doping of Nb atoms within the 3DOP-C nanofibers. To further understand the molecular structure and chemical

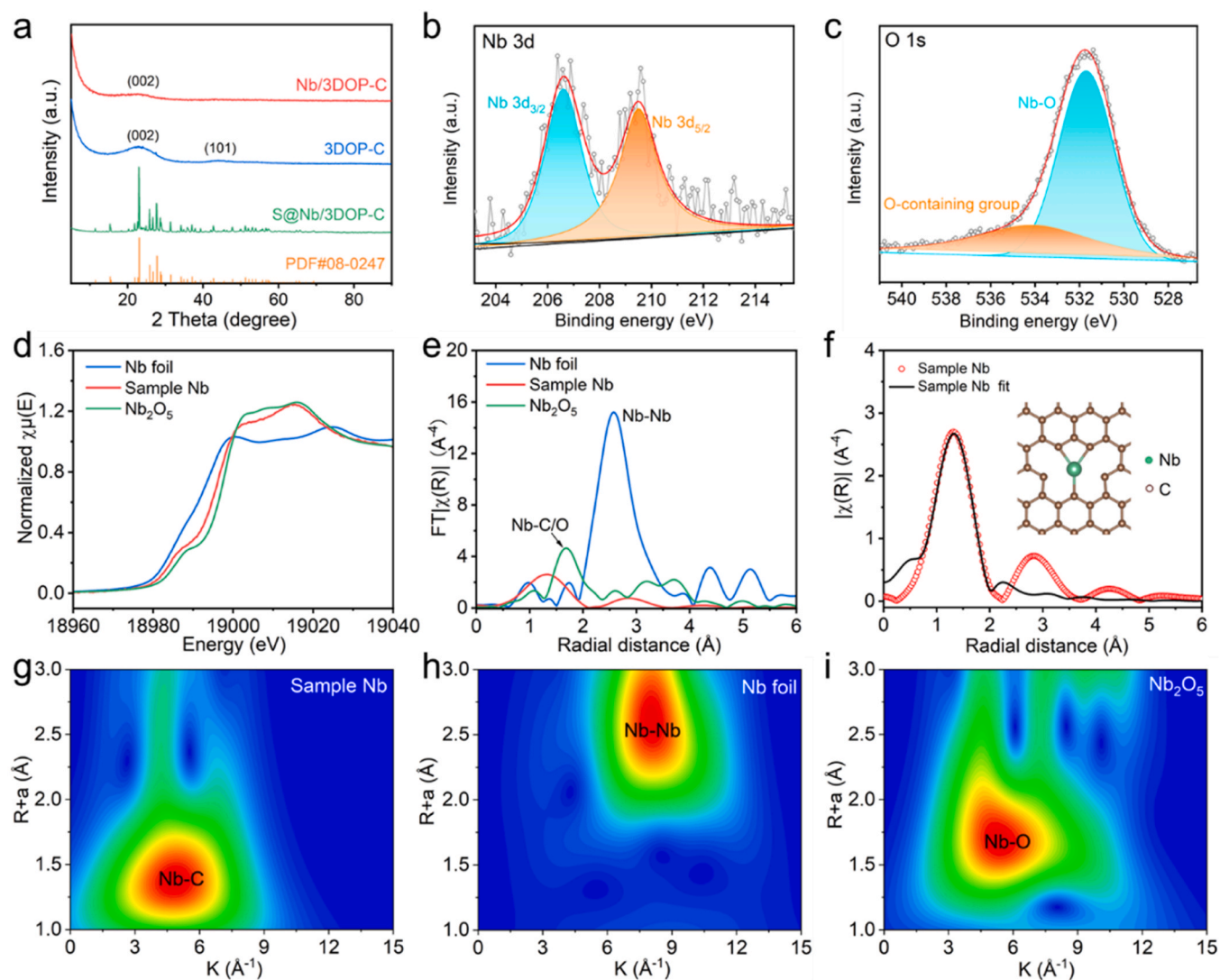


**Fig. 2.** (a) XRD patterns of Nb-SAs@3DOP-C nanofiber, 3DOP-C nanofiber and S/Nb-SAs@3DOP-C nanofiber; XPS of O (b) and Nb (c) of Nb-SAs@3DOP-C nanofiber; (d) XANES spectra at the Nb K-edge and (e) Fourier transforms of Nb K-edge EXAFS spectra of Nb sample, Nb foil, and  $\text{Nb}_2\text{O}_5$ ; (f) EXAFS fitting curves in R-space of Nb sample; Wavelet transforms for the  $k^3$ -weight Fe K-edge EXAFS information of reference samples: (g) Sample Nb; (h) Nb foil; (i)  $\text{Nb}_2\text{O}_5$ .



composition of the sample, the XPS spectrum of C 1s, O 1s, and Nb 3d spectra were shown in Figs. S7b, 2b, and 2c. The typical C and O peaks can be observed from the XPS spectra of Nb-SAs@3DOP-C (Fig. S7). From the Nb 3d spectra in composite material, it suggested that there were two distinct fitted peaks located at 209.5 eV for the Nb 3d<sub>3/2</sub> and 206.6 eV for the Nb 3d<sub>5/2</sub>; the valence state corresponds to Nb<sup>5+</sup>.

To further reveal the electronic structure and coordination environment after bonding single Nb atoms, the X-ray absorption near edge structure (XANES) and extended X-ray absorption fine structure (EXAFS) measurements were measured using Nb foil and Nb<sub>2</sub>O<sub>5</sub> as references. As shown in Fig. 2d, the near-edge structure spectrum of Nb-SAs@3DOP-C is located closer to that of Nb<sub>2</sub>O<sub>5</sub> than to Nb foil, indicating that the central element of Nb-SAs@3DOP-C exhibited a positive charge. As illustrated in Fig. 2e, the spectrum displays the dominant peak around 1.35 Å and there was no peak in the high R-space, indicating that the distribution of Nb in Nb-SAs@3DOP-C is monodisperse. In addition, a significant Nb-Nb peak located at 2.75 Å is noticed for the Nb-foil, which cannot be detected from Nb-SAs@3DOP-C. As shown in Fig. 2f and S8, the Nb-C bond with an average coordination number of 5.3 and a bond length of 2.05 Å is obtained by coordination fitting. The

EXAFS fitting parameters are shown in Table S1. To clearly examine the atom backscattering and coordination environment of Nb-SAs@3DOP-C, the wavelet transform (WT) of the Nb K-edge EXAFS signal is conducted (Figs. 2g and 2i). From the WT of the sample, it could be seen that the central region with the strongest signal moves slightly to the lower wave number compared with Nb<sub>2</sub>O<sub>5</sub>, indicating that there is no O participation in the coordination environment of the central element Nb, further demonstrating that the Nb atoms exist as mononuclear centers. These results prove that the Nb atoms are coordinated with C atoms to form Nb-C<sub>3</sub> moieties, which are atomically dispersed in 3DOP-C nanofibers.

The catalytic effect of Nb-SAs@3DOP-C composites and the adsorption behavior between Nb-C<sub>3</sub> configurations and polysulfides were further investigated through density functional theory (DFT) calculations. The optimized adsorption structures of Li<sub>2</sub>S<sub>6</sub> on Nb-SAs@3DOP-C and 3DOP-C nanofiber are displayed in Fig. 3a and S9. It could be clearly observed that Nb-SAs@3DOP-C relies on Nb-S and Li-C bonding to achieve strong polysulfide anchoring. It is noted that the adsorption energy of Li<sub>2</sub>S<sub>6</sub> on Nb-SAs@3DOP-C (-1.09 eV) is significantly stronger than that of the 3DOP-C configuration (-0.124 eV), further confirming

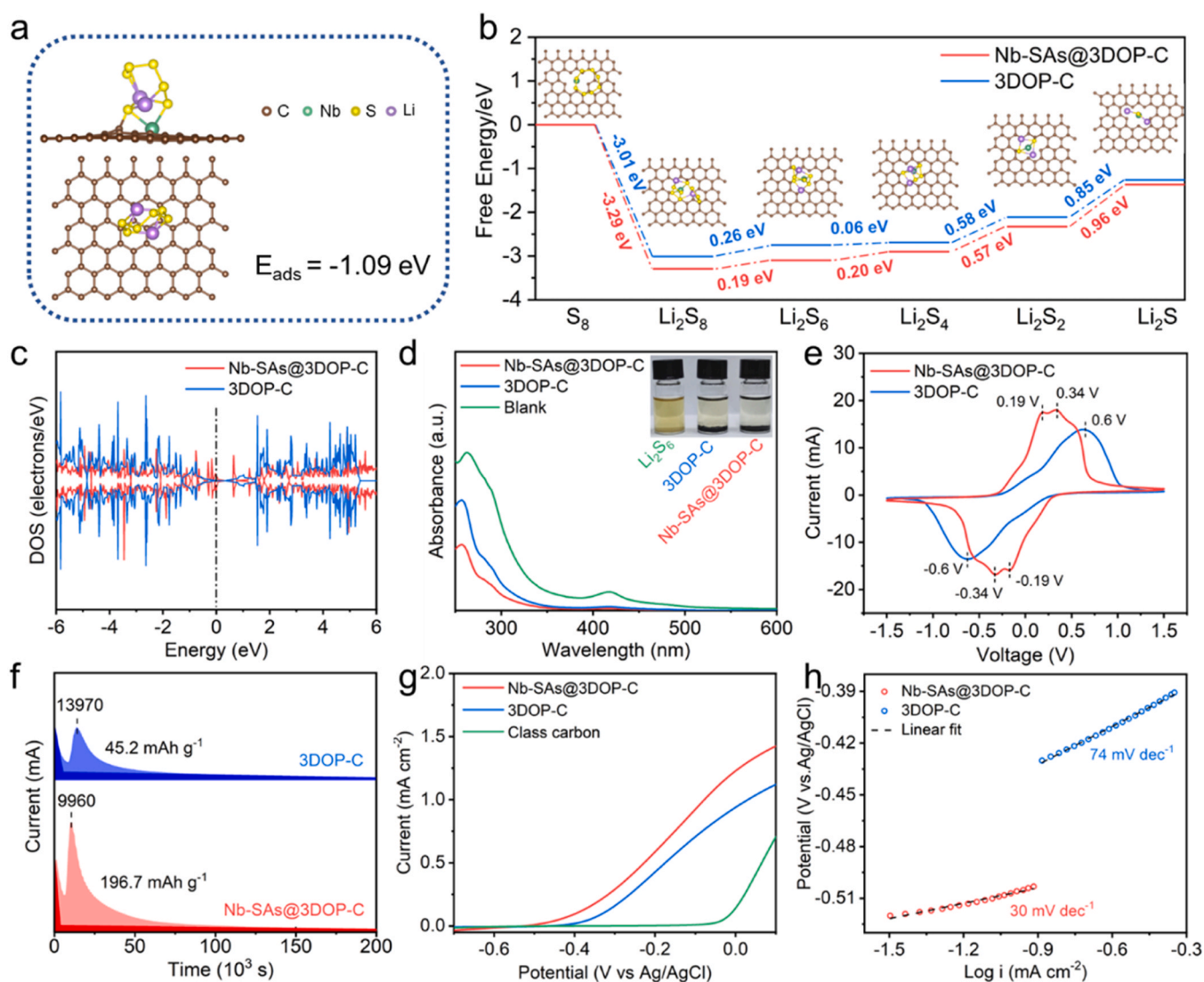


**Fig. 3.** (a) Calculated adsorption energy of Li<sub>2</sub>S<sub>6</sub> on Nb-SAs@3DOP-C; (b) The Gibbs free energy profiles of LiPSs on Nb-SAs@3DOP-C and 3DOP-C nanofiber; (inset in Fig. 3b show the optimized adsorption configurations) (c) DOS analysis; (d) UV-vis spectra and optical observation (inset) of polysulfide solution adsorbed by Nb-SAs@3DOP-C and 3DOP-C nanofiber; (e) symmetric cell of Nb-SAs@3DOP-C and 3DOP-C; (f) Li<sub>2</sub>S<sub>6</sub> precipitation profiles of Nb-SAs@3DOP-C and 3DOP-C; (g) LSV curves of Li<sub>2</sub>S oxidation, and (h) corresponding Tafel plots of Nb-SAs@3DOP-C and 3DOP-C nanofiber.

the favorable chemical adsorption behavior of the Nb-C<sub>3</sub> configuration for LiPSs species. In addition, the electron cloud density at the interfaces between Li<sub>2</sub>S<sub>6</sub> and Nb-SAs@3DOP-C (Fig. 3c) is observed, where the Nb-C<sub>3</sub> configurations exhibit more narrower bandgap near Fermi levels, indicating that Nb-SAs@3DOP-C can effectively promote electron conductivity during the redox reaction of sulfur. To further unveil the electrocatalytic function of Nb-C<sub>3</sub> configurations towards LiPSs affinity reactions, the optimized geometric configurations and Gibbs free energy profiles of the main reactions from elemental S to Li<sub>2</sub>S ( $S_8 \rightarrow Li_2S_8 \rightarrow Li_2S_6 \rightarrow Li_2S_4 \rightarrow Li_2S_2 \rightarrow Li_2S$ ) are used to be calculated in Fig. 3b. Theoretically, the larger Gibbs free energy, the slower kinetic of reaction. The reduction of solid Li<sub>2</sub>S<sub>2</sub> to solid Li<sub>2</sub>S displays the largest positive Gibbs energy barrier, suggesting that this step can be the rate-controlling in the overall sulfur reduction reaction. Considering that the reaction free-energy barrier of the rate-controlling step on Nb-SAs@3DOP-C is 0.85 eV, which is lower than that of 3DOP-C with 0.96 eV, suggesting more thermodynamically favorable deposition of Li<sub>2</sub>S. During the electrochemical reaction process, the Li<sub>2</sub>S decomposition is crucial to the whole reaction kinetics [37–39], which is tested as shown in Fig. S10. Firstly, the lithium removal processes of Li<sub>2</sub>S on different substrates 3DOP-C and Nb-SAs@3DOP-C are simulated and the corresponding energy barriers are calculated. The energy profiles of Li<sub>2</sub>S dissociation demonstrate a lower decomposition energy barrier on Nb-SAs@3DOP-C (1.40 eV) than that on 3DOP-C (1.90 eV), implying an easier dissociation of the Li<sub>2</sub>S under the regulation of Nb-C<sub>3</sub> configurations. In addition, the diffusion behavior of Li on different surfaces was also calculated, where the Nb-SAs@3DOP-C also exhibits a much lower energy barrier for Li diffusion (0.18 eV) compared with the pristine counterpart (0.22 eV). Such a low energy barrier will better meet the ionic requirements of the sulfur redox reaction.

The chemical interaction between the uniquely designed sulfur cathode material and polysulfides shows an important role in inhibiting the shuttle effect. The excellent adsorption capacity for lithium polysulfides is pivotal to solving the challenges of sulfur cathode. As shown in Fig. S11 and the inset image of Fig. 3d, the adsorption phenomena of Nb-SAs@3DOP-C and 3DOP-C nanofibers on an equal amount of Li<sub>2</sub>S<sub>6</sub> solution are studied through static adsorption experiments. The comparison by visual inspection at room temperature for 24 h clearly shows that Nb-SAs@3DOP-C composites can capture LiPSs more efficiently than that of 3DOP-C nanofibers. The interaction between LiPSs and Nb-SAs@3DOP-C was further studied by XPS analysis. In the Li 1 s spectrum of Nb-SAs@3DOP-C before and after the Li<sub>2</sub>S<sub>6</sub> adsorption (Fig. S12a), a new peak appears in the Li 1 s spectrum of Nb-SAs@3DOP-C@Li<sub>2</sub>S<sub>6</sub>, corresponding to the formation of Li-O chemical bond. The S 2p XPS spectra of Li<sub>2</sub>S<sub>6</sub> and Nb-SAs@3DOP-C@Li<sub>2</sub>S<sub>6</sub> are shown in Fig. S12b. Typically, Li<sub>2</sub>S<sub>6</sub> shows two pairs of peaks in the binding energy range of 160–166 eV, which is attributed to terminal sulfur (S<sub>T</sub><sup>1</sup>) and bridged sulfur (S<sub>B</sub><sup>0</sup>) [40,41]. It is worth noting that after adsorption on Nb-SAs@3DOP-C, these peaks change to higher binding energy, indicating that the electron cloud density of sulfur atoms decreases and the interaction with Li<sub>2</sub>S<sub>6</sub> is strong [42]. Additionally, from the UV-vis spectra, the peak intensity of Li<sub>2</sub>S<sub>6</sub> is significantly weakened after mixing lithium polysulfide and Nb-SAs@3DOP-C. This observation indicates that 3DOP-C could adsorb LiPSs to a certain extent, and the single Nb atoms embedded in the carbon matrix are more conducive to capturing and adsorbing LiPSs, further accelerating its conversion reaction.

In addition, to further investigate the catalytic mechanism of Nb-SAs@3DOP-C composite, symmetric cells with the Li<sub>2</sub>S<sub>6</sub>-contained electrolyte were assembled to study the LiPSs conversion capability. CV profiles were investigated between −1.5 and 1.5 V (Fig. 3e), where the first oxidation peak at 0.19 V for the Nb-SAs@3DOP-C symmetric cell should be assigned to the oxidation of Li<sub>2</sub>S to Li<sub>2</sub>S<sub>6</sub> on the working electrode accompanied by the reduction of elemental sulfur on the counter electrode. Similarly, the second peak at 0.34 V was due to the oxidation of Li<sub>2</sub>S<sub>6</sub> to sulfur on the working electrode and the reduction of Li<sub>2</sub>S<sub>6</sub> to Li<sub>2</sub>S on the counter electrode. The reverse processes impose two

reductive peaks at −0.19 and −0.34 V upon the cathodic scanning. By contrast, the 3DOP-C symmetric cell underwent only one pair of redox peaks at −0.6/0.6 V. As such, the sharper peak shape and lower redox overpotential strongly demonstrate the superior catalytic activity by Nb incorporation. In addition, the well-maintained CV curves of the Nb-SAs@3DOP-C electrode upon the first five cycles showed excellent stability of the conversion reaction (Fig. S13a, b). As shown in Fig. S13 (c, d), the sharp and differentiable peak doublet of Nb-SAs@3DOP-C at high scanning rates demonstrate its superior LiPSs conversion kinetics compared with 3DOP-C. The electrochemical impedance spectroscopy (EIS) plots of the symmetrical cells based on Nb-SAs@3DOP-C and 3DOP-C electrodes were depicted in Fig. S14. The results show that a concave semicircle curve at high-medium frequency is related to the interface charge transfer resistance ( $R_{ct}$ ) and the slope of the low frequency, and the Nb-SAs@3DOP-C composite exhibits the most negligible charge transfer resistance, further accelerating the conversion kinetics of LiPSs and promoting the charge transfer. Furthermore, Li<sub>2</sub>S precipitation experiments were tested on different host surfaces at 2.05 V (Fig. 3f). Compared with those of the 3DOP-C electrode (45.2 mAh g<sup>−1</sup>), the Nb-SAs@3DOP-C electrode exhibits the most intense deposition current at an earlier time point with integrated specific capacity (196.7 mAh g<sup>−1</sup>). Based on the above analysis, the atomically dispersed single Nb atoms in Nb-SAs@3DOP-C effectively reduce the energy barrier of LiPSs conversion and Li<sub>2</sub>S nucleation, accelerating the electrochemical reaction kinetics. The linear scanning voltammetry (LSV) technique was used to determine the redox reaction of Li<sub>2</sub>S (Fig. 3g) using 0.1 M Li<sub>2</sub>S/methanol as the electrolyte, and glass carbon was prepared as the control sample. It can be noted that the initial voltage of the Nb-SAs@3DOP-C electrode is −0.45 V, which is lower than the corresponding initial voltage of the 3DOP-C, due to the lower Li<sub>2</sub>S decomposition barrier of Nb-SAs@3DOP-C composite. Furthermore, compared with 3DOP-C (74 mV dec<sup>−1</sup>), the smallest Tafel slope of Nb-SAs@3DOP-C (30 mV dec<sup>−1</sup>) is more favorable for lithium-ion diffusion and sulfur redox kinetics (Fig. 3h).

To illustrate the improved electrochemical properties in S/Nb-SAs@3DOP-C compared with S/3DOP-C, the cyclic voltammogram (CV) curves in initial three cycles at a scan rate of 0.1 mV s<sup>−1</sup> were performed (Fig. 11a, d). The CV curve of the S/Nb-SAs@3DOP-C cathode shows two reduction peaks on the discharge curve at 2.28 and 2.05 V corresponding to the reduction of soluble long-chain LiPSs and the ultimately Li<sub>2</sub>S product, and one oxidation peak on the recharge curve at 2.38 V corresponding to the conversion of Li<sub>2</sub>S to S<sub>8</sub>. S/Nb-SAs@3DOP-C cathode also exhibits a stable and reversible electrochemical reaction, with all CV curves overlapping well. Fig. S15 exhibits the CV profiles and corresponding Tafel plots of S/Nb-SAs@3DOP-C and S/3DOP-C cathode with an increasing number of scan rates from 0.1 to 0.5 mV s<sup>−1</sup>, indicating that a better ion diffusion ability in the redox reaction. According to the slope of the fitting line, the S/Nb-SAs@3DOP-C electrode provides more D<sub>Li+</sub> in all the conversion states (peak A, B, and C) and involves more active materials compared with the S/3DOP-C cathode with a similar sulfur loading.

The electrochemical performance of the as-developed single atom (S/Nb-SAs@3DOP-C) catalyst was tested in coin-type Li-S batteries. Fig. 4a and Fig. S16 show the charge-discharge voltage profiles at 0.2 C for different cycles. All discharge curves contain two platforms corresponding to the formation of polysulfides at different stages, consistent with CV curves. Among them, the cell based on S/Nb-SAs@3DOP-C has a smaller polarization and a smaller overpotential due to the faster charge transfer kinetics. Fig. 4b shows a comparison of the cycling performance with different cathodes at a current density of 0.2 C. The cell with S/Nb-SAs@3DOP-C cathode exhibits a high initial capacity of 1208.1 mAh g<sup>−1</sup> and retains 849.8 mAh g<sup>−1</sup> after 100 cycles. The impressively low-capacity decay of 0.0058% per cycle shows the advantages of the unique structure of the cathode design, which is higher than that of the S/3DOP-C framework. The high cyclic stability of S/Nb-SAs@3DOP-C is ascribed to the optimized single Nb atom modified 3D

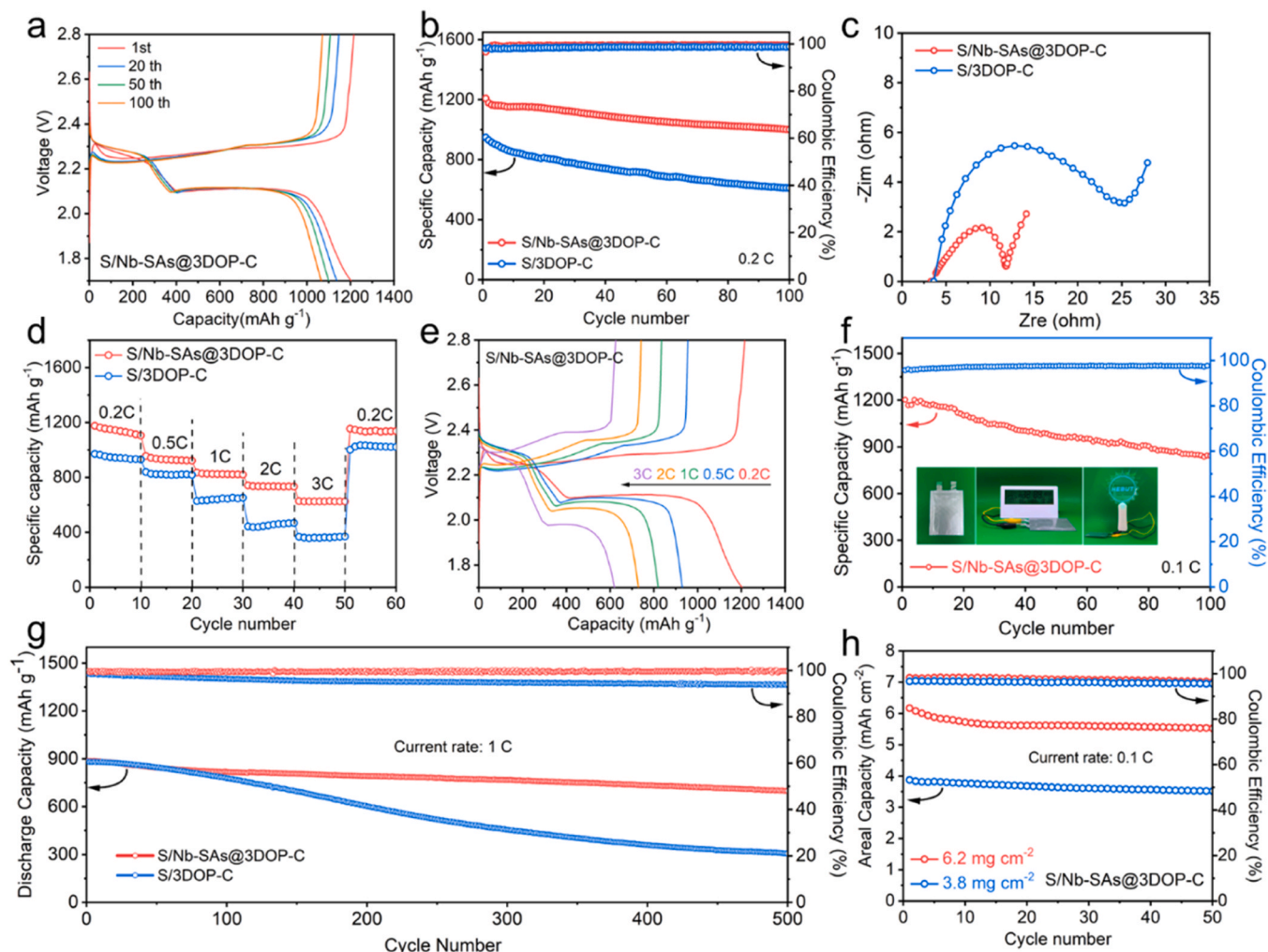


**Fig. 4.** (a) Charge-discharge curves of S/Nb-SAs@3DOP-C electrode; (b) Cycle performances at 0.2 C; (c) EIS spectra; (d) The rate performance and (e) charge-discharge profiles of S/Nb-SAs@3DOP-C from 0.2 C to 3 C; (f) the cycling performance of S/Nb-SAs@3DOP-C cathode at 0.1 C under a sulfur loading of 15 mg; (g) Cycling performance and coulombic efficiency of S/Nb-SAs@3DOP-C and S/3DOP-C electrodes at 1 C; (h) high-loading cycling performances with sulfur loadings of 3.8 and 6.2 mg cm<sup>-2</sup> at 0.1 C of S/Nb-SAs@3DOP-C cathodes.

ordered porous carbon nanofibers, which not only increases the electronic conductivity but also significantly alleviates polysulfide shuttle effect and promotes the entire sulfur redox kinetics. EIS was further conducted to observe the charge transfer resistance of electrodes, and the corresponding equivalent circuit is shown in Fig. S17. As can be seen in Nyquist plots of Fig. 4c, the S/Nb-SAs@3DOP-C electrode shows relatively lower charge transfer resistance ( $R_{ct}$ ) due to enhanced redox kinetics in the materials as a result of the doping of single Nb atoms. The rate performance of Li-S batteries with S/Nb-SAs@3DOP-C and S/3DOP-C cathodes were also evaluated at current densities ranging from 0.2 to 3 C, and then back to 0.2 C. Fig. 4d illustrates the reversible capacity of the batteries with S/Nb-SAs@3DOP-C cathode, which exhibits a significant increase in capacity compared to S/3DOP-C cathode, delivering a discharge capacity of 1176.0, 955.9, 835.7, 741.8, and 627.7 mAh g<sup>-1</sup> at 0.2, 0.5, 1, 2, and 3 C respectively. Further, a high discharge capacity of 1053.9 mAh g<sup>-1</sup> is recovered when the rate is resumed back to 0.2 C, which indicates the fast conversion kinetics and excellent catalytic effect of sulfur redox reactions. The corresponding charge-discharge voltage profiles of S/Nb-SAs@3DOP-C and S/3DOP-C electrodes at various rates are shown in Fig. 4e and Fig. S18. The more prolonged and stable discharge plateaus at various current rates imply excellent rate capability and good redox reaction kinetics.

As shown in Fig. 4f, the Li-S pouch cell with S/Nb-SAs@3DOP-C

cathode was also fabricated and tested at a sulfur loading of 15 mg, showing a high specific capacity of 967.2 mAh g<sup>-1</sup> after 100 cycles at 0.1 C. Even after 100 cycles, the pouch cell can easily power electronic clocks and handheld models. The excellent cycle stability of S/Nb-SAs@3DOP-C is better than expected, which provides broad prospects for the practical application of Li-S batteries. The S/Nb-SAs@3DOP-C electrode is then tested for prolonged cycling lifetime (Fig. 4g), which delivers a high reversible capacity of 886.6 mAh g<sup>-1</sup> with a capacity decay rate of only 0.012% per cycle after 500 cycles at 1 C. Compared with S/3DOP-C, S/Nb-SAs@3DOP-C shows very promising extended cycle life and high capacity retention. These results indicate that the modification of single Nb atoms in composites can significantly stabilize and accelerate the redox reaction, which can effectively improve the electrochemical performance and reaction kinetics of Li-S batteries. The high electrochemical performance of Li-S batteries under high sulfur loading is crucial for practical applications of high-energy-density Li-S batteries due to the increased shuttle effect. As displayed in Fig. 4h, when the electrode with a loading of 6.2 mg cm<sup>-2</sup> and 3.8 mg cm<sup>-2</sup>, the areal capacity of S/Nb-SAs@3DOP-C cell at 0.1 C is 5.52 mAh cm<sup>-2</sup> and 3.51 mAh cm<sup>-2</sup>. These outcomes demonstrate the effectiveness of S/Nb-SAs@3DOP-C cathode in suppressing the shuttle effect of polysulfides and elevating the cycle performance of Li-S batteries under high sulfur loading.



### 3. Conclusions

In summary, the uniform dispersal of embedding Nb SAs on 3D ordered porous carbon nanofibers was synthesized by template strategy as advanced host for sulfur cathode material in Li-S batteries. Introducing Nb SAs can modify 3D-ordered porous carbon nanofibers with excellent synergistic catalysis, enhancing chemical adsorption with LiPSs, and hinder the shuttling of negatively charged polysulfides. The obtained S/Nb-SAs@3DOP-C cathode demonstrates excellent electrochemical performance with a higher initial discharging capacity of 1208.1 mAh g<sup>-1</sup> at 0.2 C and low capacity decay of 0.012% per cycle at 1.0 C for 500 cycles. This work provides a promising ordered mesoporous strategy with the single atom catalyst as a sulfur host for Li-S batteries, and advances the research on high energy density and long-life rechargeable cathode for Li-S batteries.

### CRediT authorship contribution statement

**Yan Wang:** Investigation, Formal analysis. **Tongbin Zhang:** Investigation. **Lining Pan:** Writing – review & editing, Visualization, Supervision. **Jiabin Liu:** Writing – review & editing, Formal analysis. **Chuyin Ma:** Writing – review & editing, Investigation, Formal analysis. **Tingzhou Yang:** Writing – review & editing, Visualization, Validation, Methodology, Formal analysis. **Zhongwei Chen:** Supervision, Visualization, Writing – review & editing. **Shufeng Jia:** Writing – review & editing, Writing – original draft, Validation, Methodology, Investigation, Formal analysis, Data curation, Conceptualization. **Shupeng Zhao:** Writing – review & editing, Writing – original draft, Visualization, Validation, Methodology, Investigation. **Yongguang Zhang:** Writing – review & editing, Visualization, Supervision, Funding acquisition. **Zijiang Xu:** Formal analysis, Investigation, Writing – review & editing. **Xia Sun:** Formal analysis. **Ning Liu:** Writing – review & editing, Visualization, Supervision.

### Declaration of Competing Interest

The authors declare that they have no known competing financial interests or personal relationships that could have appeared to influence the work reported in this paper.

### Data Availability

Data will be made available on request.

### Acknowledgments

The authors would like to acknowledge the financial support from Natural Science Foundation of Hebei Province, China (B2021202028, B2020202052); Program for the Outstanding Young Talents of Hebei Province, China.

### Appendix A. Supporting information

Supplementary data associated with this article can be found in the online version at [doi:10.1016/j.apcatb.2024.124012](https://doi.org/10.1016/j.apcatb.2024.124012).

### References

- [1] Y. Yuan, D. Zheng, H. Lu, et al., A multifunctional gel coating design for simultaneous interface amelioration, polysulfide adsorption and redox regulation in lithium-sulfur batteries, *Appl. Surf. Sci.* 533 (2020) 147490, <https://doi.org/10.1016/j.apsusc.2020.147490>.
- [2] S. Lou, Z. Yu, Q. Liu, et al., Multi-scale imaging of solid-state battery interfaces: from atomic scale to macroscopic scale, *Chem* 6 (9) (2020) 2199–2218, <https://doi.org/10.1016/j.chempr.2020.06.030>.
- [3] K. Han, T. Wang, N. Zhang, et al., A film coating assembled by tubular nitrogen-doped carbon fibers as an efficient membrane spacer to suppress the shuttle effect for long-life lithium-sulfur batteries, *Electrochim. Acta* 365 (2021) 137232, <https://doi.org/10.1016/j.electacta.2020.137232>.
- [4] Y. Zhang, J. Ren, Y. Zhao, et al., A porous 3D-RGO@MWCNT hybrid material as Li-S battery cathode, *Beilstein J. Nanotechnol.* 10 (1) (2019) 514–521, <https://doi.org/10.3762/bjnano.10.52>.
- [5] S.D. Seo, D. Park, S. Park, et al., “Brain-coral-like” mesoporous hollow CoS<sub>2</sub>@N-doped graphitic carbon nanoshells as efficient sulfur reservoirs for lithium-sulfur batteries, *Adv. Funct. Mater.* 29 (38) (2019) 1903712, <https://doi.org/10.1002/adfm.201903712>.
- [6] Y. Zhang, W. Qiu, Y. Zhao, et al., Ultra-fine zinc oxide nanocrystals decorated three-dimensional macroporous polypyrrole inverse opal as efficient sulfur hosts for lithium/sulfur batteries, *Chem. Eng. J.* 375 (2019) 122055, <https://doi.org/10.1016/j.cej.2019.122055>.
- [7] X. Liu, S. Wang, A. Wang, et al., A new cathode material synthesized by a thiol-modified metal-organic framework (MOF) covalently connecting sulfur for superior long-cycling stability in lithium-sulfur batteries, *J. Mater. Chem. A* 7 (42) (2019) 24515–24523, <https://doi.org/10.1039/C9TA08043K>.
- [8] J. Ren, Z. Song, X. Zhou, et al., A porous carbon polyhedron/carbon nanotube based hybrid material as multifunctional sulfur host for high-performance lithium-sulfur batteries, *ChemElectroChem* 6 (13) (2019) 3410–3419, <https://doi.org/10.1002/celec.201900744>.
- [9] X. Gao, S. Li, Y. Du, et al., A ZIF-67-derived-sulfur sandwich structure for high performance Li-S batteries, *APL Mater.* 7 (9) (2019) 091115, <https://doi.org/10.1063/1.5122819>.
- [10] A.A. Razzaq, X. Yuan, Y. Chen, et al., Anchoring MOF-derived CoS<sub>2</sub> on sulfurized polyacrylonitrile nanofibers for high areal capacity lithium-sulfur batteries, *J. Mater. Chem. A* 8 (3) (2020) 1298–1306, <https://doi.org/10.1039/C9TA11390H>.
- [11] T. Wang, G. Cui, Y. Zhao, et al., Porous carbon nanotubes microspheres decorated with strong catalyst cobalt nanoparticles as an effective sulfur host for lithium-sulfur battery, *J. Alloy. Compd.* 853 (2021) 157268, <https://doi.org/10.1016/j.jallcom.2020.157268>.
- [12] N. Wang, J. Wang, J. Zhao, et al., Synthesis of porous-carbon@ reduced graphene oxide with superior electrochemical behaviors for lithium-sulfur batteries, *J. Alloy. Compd.* 851 (2021) 156832, <https://doi.org/10.1016/j.jallcom.2020.156832>.
- [13] D. Cheng, Y. Zhao, X. Tang, et al., Densely integrated Co, N-Codoped Graphene@Carbon nanotube porous hybrids for high-performance lithium-sulfur batteries, *Carbon* 149 (2019) 750–759, <https://doi.org/10.1016/j.carbon.2019.04.108>.
- [14] S. Chen, J. Luo, N. Li, et al., Multifunctional LDH/Co<sub>9</sub>S<sub>8</sub> heterostructure nanocages as high-performance lithium/sulfur battery cathodes with ultralong lifespan, *Energy Storage Mater.* 30 (2020) 187–195, <https://doi.org/10.1016/j.ensm.2020.05.002>.
- [15] P. Chen, T. Wang, D. He, et al., Delocalized isoelectronic heterostructured FeCoO<sub>x</sub>S<sub>y</sub> catalysts with tunable electron density for accelerated sulfur redox kinetics in Li-S batteries, *Angew. Chem.* 135 (47) (2023) e202311693, <https://doi.org/10.1002/anie.202311693>.
- [16] J. Wang, L. Li, H. Hu, et al., Toward dendrite-free metallic lithium anodes: from structural design to optimal electrochemical diffusion kinetics, *ACS Nano* 16 (11) (2022) 17729–17760, <https://doi.org/10.1021/acsnano.2c08480>.
- [17] C. Luo, E. Hu, K.J. Gaskell, et al., A chemically stabilized sulfur cathode for lean electrolyte lithium sulfur batteries, *Proc. Natl. Acad. Sci. USA* 117 (26) (2020) 14712–14720, <https://doi.org/10.1073/pnas.2006301117>.
- [18] J. Zhou, T. Wu, Y. Pan, et al., Packing sulfur species by phosphorene-derived catalytic interface for electrolyte-lean lithium-sulfur batteries, *Adv. Funct. Mater.* 32 (4) (2022) 2106966, <https://doi.org/10.1002/adfm.202106966>.
- [19] T. Lei, W. Chen, W. Lv, et al., Inhibiting polysulfide shuttling with a graphene composite separator for highly robust lithium-sulfur batteries, *2018, Joule* 2 (10) (2018) 2091–2104, <https://doi.org/10.1016/j.joule.2018.07.022>.
- [20] L.L. Kong, L. Wang, Z.C. Ni, et al., Lithium-magnesium alloy as a stable anode for lithium-sulfur battery, *Adv. Funct. Mater.* 29 (13) (2019) 1808756, <https://doi.org/10.1002/adfm.201808756>.
- [21] F. Pei, A. Fu, W. Ye, et al., Robust lithium metal anodes realized by lithiophilic 3D porous current collectors for constructing high-energy lithium-sulfur batteries, *ACS Nano* 13 (7) (2019) 8337–8346, <https://doi.org/10.1021/acsnano.9b03784>.
- [22] J. He, A. Bhargava, H. Yaghoobnejad Asl, et al., 1T'-ReS<sub>2</sub> nanosheets in situ grown on carbon nanotubes as a highly efficient polysulfide electrocatalyst for stable Li-S batteries, *Adv. Energy Mater.* 10 (23) (2020) 2001017, <https://doi.org/10.1002/aenm.202001017>.
- [23] Y. Li, C. Wang, W. Wang, et al., Enhanced chemical immobilization and catalytic conversion of polysulfide intermediates using metallic Mo nanoclusters for high-performance Li-S batteries, *ACS Nano* 14 (1) (2019) 1148–1157, <https://doi.org/10.1021/acsnano.9b09135>.
- [24] J.S. Yeon, Y.H. Ko, T.H. Park, et al., Multidimensional hybrid architecture encapsulating cobalt oxide nanoparticles into carbon nanotube branched nitrogen-doped reduced graphene oxide networks for lithium-sulfur batteries, *Energy Environ. Mater.* 5 (2) (2022) 555–564, <https://doi.org/10.1002/eeem.2.12187>.
- [25] T. Wang, G. Cui, Y. Zhao, et al., Porous carbon nanotubes microspheres decorated with strong catalyst cobalt nanoparticles as an effective sulfur host for lithium-sulfur battery, *J. Alloy. Compd.* 853 (2021) 157268, <https://doi.org/10.1016/j.jallcom.2020.157268>.
- [26] C.L. Song, G.H. Li, Y. Yang, et al., 3D catalytic MOF-based nanocomposite as separator coatings for high-performance Li-S battery, *Chem. Eng. J.* 381 (2020) 122701, <https://doi.org/10.1016/j.cej.2019.122701>.
- [27] Y.J. Li, J.B. Wu, B. Zhang, et al., Fast conversion and controlled deposition of lithium (poly) sulfides in lithium-sulfur batteries using high-loading cobalt single

- atoms, *Energy Storage Mater.* 30 (2020) 250–259, <https://doi.org/10.1016/j.ensm.2020.05.022>.
- [28] L. Zhang, D. Liu, Z. Muhammad, et al., Single nickel atoms on nitrogen-doped graphene enabling enhanced kinetics of lithium-sulfur batteries, *Adv. Mater.* 31 (40) (2019) 1903955, <https://doi.org/10.1002/adma.201903955>.
- [29] J. Wang, J. Zhang, J. Wu, et al., Interfacial “single-atom-in-defects” catalysts accelerating  $\text{Li}^+$  desolvation kinetics for long-lifespan lithium-metal batteries, *Adv. Mater.* 35 (39) (2023) 2302828, <https://doi.org/10.1002/adma.202302828>.
- [30] J. Wang, J. Zhang, S. Duan, et al., Lithium atom surface diffusion and delocalized deposition propelled by atomic metal catalyst toward ultrahigh-capacity dendrite-free lithium anode, *Nano Lett.* 22 (19) (2022) 8008–8017, <https://doi.org/10.1021/acs.nanolett.2c02611>.
- [31] J. Wang, J. Zhang, S. Cheng, et al., Long-life dendrite-free lithium metal electrode achieved by constructing a single metal atom anchored in a diffusion modulator layer, *Nano Lett.* 21 (7) (2021) 3245–3253, <https://doi.org/10.1021/acs.nanolett.1c00534>.
- [32] C. Ren, Q. Jiang, W. Lin, et al., Density functional theory study of single-atom V, Nb, and Ta catalysts on graphene and carbon nitride for selective nitrogen reduction, *ACS Appl. Nano Mater.* 3 (6) (2020) 5149–5159, <https://doi.org/10.1021/acsanm.0c00512>.
- [33] Y. Zhang, C. Kang, W. Zhao, et al., d-p hybridization-induced “trapping-coupling-conversion” enables high-efficiency Nb single-atom catalysis for Li-S batteries, *J. Am. Chem. Soc.* 145 (3) (2023) 1728–1739, <https://doi.org/10.1021/jacs.2c10345>.
- [34] Y. Zhang, W. Zhao, C. Kang, et al., Phase-junction engineering triggered built-in electric field for fast-charging batteries operated at  $-30^\circ\text{C}$ , *Matter* 6 (6) (2023) 1928–1944, <https://doi.org/10.1016/j.matt.2023.03.026>.
- [35] S. Lou, X. Cheng, Y. Zhao, et al., Superior performance of ordered macroporous  $\text{TiNb}_2\text{O}_7$  anodes for lithium ion batteries: understanding from the structural and pseudocapacitive insights on achieving high rate capability, *Nano Energy* 34 (2017) 15–25, <https://doi.org/10.1016/j.nanoen.2017.01.058>.
- [36] Y. Liu, Z. Wei, B. Zhong, et al., O-, N-Coordinated single Mn atoms accelerating polysulfides transformation in lithium-sulfur batteries, *Energy Storage Mater.* 35 (2021) 12–18, <https://doi.org/10.1016/j.ensm.2020.11.011>.
- [37] J. Wang, L. Jia, J. Zhong, et al., Single-atom catalyst boosts electrochemical conversion reactions in batteries, *Energy Storage Mater.* 18 (2019) 246–252, <https://doi.org/10.1016/j.ensm.2018.09.006>.
- [38] J. Wang, L. Jia, S. Duan, et al., Single atomic cobalt catalyst significantly accelerates lithium ion diffusion in high mass loading  $\text{Li}_2\text{S}$  cathode, *Energy Storage Mater.* 28 (2020) 375–382, <https://doi.org/10.1016/j.ensm.2020.03.023>.
- [39] J. Zhang, C. You, H. Lin, et al., Electrochemical kinetic modulators in lithium-sulfur batteries: from defect-rich catalysts to single atomic catalysts, *Energy Environ. Mater.* 5 (3) (2022) 731–750, <https://doi.org/10.1002/eem2.12250>.
- [40] G. Li, W. Lei, D. Luo, et al., Stringed “tube on cube” nanohybrids as compact cathode matrix for high-loading and lean-electrolyte lithium-sulfur batteries, *Energy Environ. Sci.* 11 (9) (2018) 2372–2381, <https://doi.org/10.1039/c8ee01377b>.
- [41] X. Wang, D. Luo, J. Wang, et al., Strain engineering of a MXene/CNT hierarchical porous hollow microsphere electrocatalyst for a high-efficiency lithium polysulfide conversion process, *Angew. Chem. Int. Ed.* 60 (5) (2021) 2371–2378, <https://doi.org/10.1002/anie.202011493>.
- [42] G. Li, F. Lu, X. Dou, et al., Polysulfide regulation by the zwitterionic barrier toward durable lithium-sulfur batteries, *J. Am. Chem. Soc.* 142 (7) (2020) 3583–3592, <https://doi.org/10.1021/jacs.0c08537>.